Available on the CERN CDS information server **CMS PAS SUS-19-013**

# CMS Physics Analysis Summary

Contact: cms-pag-conveners-susy@cern.ch 2020/05/25

# Search for supersymmetry in proton-proton collisions at $\sqrt{s} = 13$ TeV in final states with high-momentum Z bosons and missing transverse momentum

The CMS Collaboration


## Abstract

A search for physics beyond the standard model in events with highly Lorentz-boosted Z bosons and missing transverse momentum is presented. The analysed proton-proton collision data, corresponding to an integrated luminosity of 137 fb$^{-1}$, were recorded at $\sqrt{s} = 13$ TeV by the CMS experiment. The search utilizes wide-cone jets to identify quark pairs from Z boson decays. Backgrounds from standard model processes are suppressed by requirements on the jet mass and missing transverse momentum. No significant excess in the event yield is observed beyond the number of background events expected from the standard model. An exclusion limit on the mass of gluinos - supersymmetric partners of gluons - as large as 1920 GeV is set at 95% confidence level within the framework of simplified model spectra.

# 1 Introduction

The discovery of a Higgs boson in 2012 by the CMS and ATLAS experiments [1, 2] at the CERN LHC fulfilled the predicted particle content of the standard model (SM). Within this theoretical framework, however, the Higgs boson mass of around 125 GeV presents a special challenge as the calculated mass is unstable against corrections from quantum loop processes. In the absence of extreme fine-tuning [3–6] that would precisely cancel the divergent terms, the mass value can run up to the Planck scale as a cutoff. This instability of the Higgs boson mass and the entire electroweak scale is known as the gauge hierarchy problem.

One widely studied extension of the SM is supersymmetry (SUSY) [7–9], which posits a partner for each SM particle differing in spin by one-half unit. For example, squarks $\widetilde{q}$ and gluinos $\widetilde{g}$ are the SUSY partners of quarks and gluons, respectively. Depending on the mass hierarchy of these new particles, they could resolve the gauge hierarchy problem by providing necessary radiative corrections to offset the SM contributions. Furthermore, in $R$-parity [10, 11] conserving models, SUSY particles are produced in pairs while the lightest of them is neutral, stable and weakly interacting. This lightest SUSY particle (LSP), provides a suitable candidate for dark matter [11], which is not described by known fields in the SM. The typical experimental signatures of pair-produced SUSY particle decay chains are jets, leptons and large missing transverse momentum ($p_{\mathrm{T}}^{\mathrm{miss}}$).

As gluinos and squarks carry color charges, like their SM partners, they can be produced via the strong interaction; they therefore have the highest production cross sections among SUSY particles for a given mass. Searches for direct decays of gluinos to quarks lead to lower limits of $m_{\widetilde{g}} \approx 2\,\mathrm{TeV}$ depending on the model. This search focuses on gluino decay cascades to Z bosons and the LSP via the next-to-lightest SUSY particle, NLSP. We consider a SUSY picture in which the NLSP and LSP are respectively the scalar neutralinos $\tilde{\chi}_2^0$ and $\tilde{\chi}_1^0$, mixed states of partners of the neutral Higgs and gauge bosons. We further assume a small mass splitting between the $\widetilde{g}$ and $\tilde{\chi}_2^0$, and a light $\tilde{\chi}_1^0$. This gives rise to energetic Z bosons along with large $p_{\mathrm{T}}^{\mathrm{miss}}$ and additional soft quarks in the final state. In our model calculations we set the $\tilde{\chi}_1^0$ mass to 1 GeV and the difference in mass between the $\widetilde{g}$ and $\tilde{\chi}_2^0$ to 50 GeV. For the dominant $\mathrm{Z} \to \mathrm{q}\overline{\mathrm{q}}$ decay at large momentum, the decay products can be contained in a single reconstructed jet with a large radius (wide-cone jet). Figure 1 shows the SUSY process targeted by this search within the framework of simplified model spectra (SMS) [12–15], referred to as T5ZZ. Such models are inspired by “natural” SUSY scenarios like those described in Ref. [16], which result in minimal fine-tuning of the SM to solve the gauge hierarchy problem, and give experimental signatures with vector bosons and $p_{\mathrm{T}}^{\mathrm{miss}}$ in the final state.

In this note, we present a search in proton-proton (pp) collisions at $\sqrt{s} = 13\,\mathrm{TeV}$ for events with two highly Lorentz-boosted, hadronically decaying Z bosons and large $p_{\mathrm{T}}^{\mathrm{miss}}$. The analysis is based on the Run-2 data set with an integrated luminosity of $137\,\mathrm{fb}^{-1}$, recorded by the CMS experiment during 2016-2018. The signal signature is a pair of wide-cone jets each having a reconstructed mass consistent with the Z boson mass. This selection in combination with large $p_{\mathrm{T}}^{\mathrm{miss}}$ greatly suppresses backgrounds from SM processes. This is the first search performed for the pair production of gluinos in this specific topology.

# 2 CMS detector and trigger

A detailed description of the CMS detector and the associated coordinate system and kinematic variables are given in Ref. [17]. The main components of the apparatus are briefly discussed here. CMS is a cylindrical superconducting solenoid with an inner diameter of 6 m that pro-

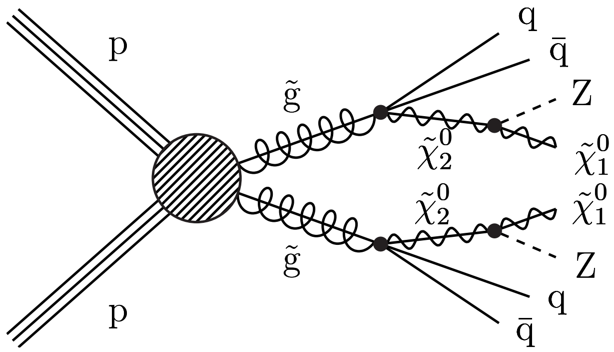


Figure 1: Signal diagram for the T5ZZ SMS process. The assumed small mass splitting between the $\tilde{g}$ and $\tilde{\chi}_2^0$ implies a massive $\tilde{\chi}_2^0$. We further assume a 100% branching fraction for the $\tilde{\chi}_2^0$ decay to the Z boson and $\tilde{\chi}_1^0$, leading to a high-momentum Z boson and large $p_T^{miss}$.

vides a 3.8 T axial magnetic field. A silicon pixel and strip tracker, a lead tungstate crystal electromagnetic calorimeter, and a brass and scintillator hadron calorimeter are placed within the cylindrical volume. Gas-ionization detectors are embedded in the steel flux-return yoke outside the solenoid to identify muons. The detector is nearly hermetic, permitting accurate measurements of $p_T^{miss}$.

The CMS trigger system is described in Ref. [18]. For this analysis, signal candidate events were recorded by requiring $p_T^{miss}$ at the trigger level to exceed a threshold that varied between 100 and 120 GeV, depending on the LHC instantaneous luminosity. The efficiency of this trigger is measured in data to be greater than 97% for events satisfying the selection criteria described in Section 5 below. Additional triggers are used to select control samples for the background predictions.

## 3 Simulation event samples

The estimation of background (Section 6) is primarily based on data in control regions. Samples of Monte Carlo (MC) simulated events are used to test the background techniques as well as to optimize the selection criteria. These samples include events with top quark pair production ($t\bar{t}$), and photon, W boson, or Z boson production accompanied by jets, denoted $\gamma$+jets, W+jets, or Z+jets, respectively.

The SM production of $t\bar{t}$, $\gamma$+jets, W+jets, Z+jets, and quantum chromodynamics (QCD) multijet events is simulated using the MADGRAPH5_aMC@NLO 2.2.2 [19, 20] generator for 2016 samples and MADGRAPH5_aMC@NLO 2.4.2 for 2017 and 2018 samples, all with leading order (LO) precision. The $t\bar{t}$ events are generated with up to three additional partons in the matrix element calculations, while the $\gamma$+jets, W+jets, and Z+jets events are generated with up to four additional partons. Single top quark events produced via the $s$ channel, diboson events originating from WW, ZZ, or ZH production (where H denotes a Higgs boson), and rare events from $t\bar{t}$W, $t\bar{t}$Z, and WWZ production, are generated with MADGRAPH5_aMC@NLO 2.2.2 at next-to-leading order (NLO) [21], except that WW events in which both W bosons decay leptonically are generated using the POWHEG v2.0 [22–26] program at NLO. The same POWHEG generator is used to describe single top quark events produced through the $t$ and tW channels. The detector response is modeled with GEANT4 [27]. Normalization of the simulated background samples is performed using the most accurate cross section calculations available [19, 25, 26, 28–36], which generally correspond to NLO or next-to-NLO (NNLO) precision.

Samples of simulated signal events are generated at LO using MADGRAPH5_aMC@NLO 2.2.2

(2.4.2) for the 2016 (2017 and 2018) samples, with up to two additional partons included in the matrix element calculations. The production cross sections are determined with approximate NNLO plus next-to-next-to-leading logarithmic (NNLL) precision [37–48].

All simulated samples make use of the PYTHIA 8.205 [49] program to describe parton showering and hadronization. The CUETP8M1 [50] PYTHIA 8.205 tune was used to produce both the SM background and signal samples for the 2016 simulation. In the case of the 2017 and 2018 simulation, PYTHIA 8.230 is used with the CP5 tune [51] implemented for background samples and the CP2 tune [51] for signal samples. Simulated samples generated at LO (NLO) with the CUETP8M1 tune use the NNPDF2.3LO (NNPDF2.3NLO) [52] parton distribution function (PDF) set, while those using the CP2 or CP5 tune use the NNPDF3.1LO (NNPDF3.1NNLO) [53] PDF set. The simulated events are generated with a distribution of pp interactions per bunch crossing ("pileup") that is adjusted to match the corresponding distribution measured in data.

To improve the description of initial-state radiation (ISR), the MADGRAPH5_aMC@NLO prediction is compared to data in a control region enriched in $t\bar{t}$ events for deriving a correction factor. The factor is subsequently applied to simulated $t\bar{t}$ and signal events so that the ISR jet distribution agrees with that in data. The correction is found to be unnecessary for $t\bar{t}$ samples that are generated with the CP5 tune, so it is not applied to those samples.

# 4 Event reconstruction

Individual particles are reconstructed with the CMS particle-flow (PF) algorithm [54], which identifies them as photons, charged and neutral hadrons, electrons, or muons. These objects are characterized kinematically by their transverse momentum $p_T$, pseudorapidity $\eta$, and azimuthal angle $\phi$. Photon and electron candidates are restricted to the pseudorapidity range $|\eta| < 2.5$, and muon candidates to $|\eta| < 2.4$, within the fiducial coverage of the tracking and muon system, respectively.

The reconstructed vertex with the largest value of summed physics-object $p_T^2$ is taken to be the primary pp interaction vertex, where the physics objects are the jets, clustered using the anti-$k_T$ algorithm [55, 56] with the charged particle tracks assigned to the vertex as inputs, and the associated missing transverse momentum, taken as the negative vector sum of the $p_T$ of those jets. Charged particle tracks associated with vertices other than the primary one are removed from further consideration. The primary vertex is required to lie within 24 cm of the center of the detector in the direction along the beam axis and within 2 cm in the plane transverse to that axis.

Jets are defined as clusters of PF candidates formed by the anti-$k_T$ algorithm. Quality criteria [57, 58] are imposed to suppress jets from spurious sources such as electronics noise. The jet energies are corrected for the nonlinear response of the detector [59]. Jets with $p_T > 30$ GeV, $|\eta| < 2.4$ and a distance parameter of 0.4 (AK4) are used to calculate some of the selection variables. For these jets, charged particles that emerge from vertices other than the primary one are removed from the list of PF candidates used for the jet clustering. The expected contribution from neutral particles from pileup is removed using the effective area technique [60]. On the other hand, wide-cone jets with $p_T > 200$ GeV and a distance parameter of 0.8 (AK8) are used to reconstruct the Z boson decays. These AK8 jets are reclustered from their original constituents using the "soft-drop" method [61] to remove wide-angle radiation that can adversely impact the mass measurement of the jet. Contributions from pileup in AK8 jets are removed with the PUPPI technique [62]. The soft-drop mass $m_{jet}$ is then used to identify jets from $Z \to q\bar{q}$ decays.

The identification of b jets (b-jet tagging) is performed by applying, to the AK4 jet sample, a version of the combined secondary vertex algorithm based on deep neural networks [63]. The medium working point of this algorithm is used. The tagging efficiency for b jets with $p_{\mathrm{T}} \approx 30\,\mathrm{GeV}$ is 65%. The corresponding misidentification probability for gluon and light-flavor quark jets is 1.6% while that for charm quark jets is 13%.

As described in Section 5 below, events with leptons or photons are excluded from the search samples. Electron and muon candidates are identified as described in Refs. [64] and [65], respectively, using the "veto" working points. To suppress jets erroneously identified as leptons or genuine leptons from hadron decays, electron and muon candidates are subjected to an isolation requirement. The isolation criterion is based on a variable $I$, which is the scalar $p_{\mathrm{T}}$ sum of charged hadron, neutral hadron, and photon PF candidates within a cone of radius $\Delta R = \sqrt{(\Delta\phi)^2 + (\Delta\eta)^2}$ around the lepton direction, divided by the lepton $p_{\mathrm{T}}$. The expected contributions of neutral particles from pileup are subtracted [60]. The radius of the cone is 0.2 for lepton $p_{\mathrm{T}} < 50\,\mathrm{GeV}$, $10\,\mathrm{GeV}/p_{\mathrm{T}}$ for $50 \leq p_{\mathrm{T}} \leq 200\,\mathrm{GeV}$, and 0.05 for $p_{\mathrm{T}} > 200\,\mathrm{GeV}$. The decrease in cone size with increasing lepton $p_{\mathrm{T}}$ accounts for the increased collimation of the decay products from the lepton's parent particle as the Lorentz boost of the latter increases [66]. The isolation requirement is $I < 0.1$ (0.2) for electrons (muons).

To further suppress events with leptons from hadron decays and single-prong hadronic $\tau$ lepton decays, charged particle tracks not identified as electrons or muons by the criteria of the previous paragraph are added to the event selection veto. For these candidates the scalar $p_{\mathrm{T}}$ sum of all other charged particle tracks within a cone of radius 0.3 around the track direction, divided by the track $p_{\mathrm{T}}$, is required to be less than 0.2 if the track is identified as a PF electron or muon and less than 0.1 otherwise. Isolated tracks are required to satisfy $|\eta| < 2.4$.

Photon candidates are identified as described in Ref. [67], using the "veto" working point, and with an isolation requirement based on the individual sums of energy from charged and neutral hadrons and electromagnetically interacting particles, excluding the photon candidate itself, within a cone of radius $\Delta R = 0.3$ around the photon candidate's direction, corrected for pileup [67]. Each of the three individual sums is required not to exceed a threshold that depends on the calorimeter geometry.

## 5 Event selection

We select events with large values of jet activity and of missing transverse momentum, no leptons, and wide-cone jets from Lorentz boosted, hadronically decaying Z bosons. Control regions for the determination of backgrounds are also defined.

The observables used to characterize candidate events are:

- $N_{\mathrm{jet}}$, the number of AK4 jets in the event;
- $\vec{p}_{\mathrm{T}}^{\mathrm{miss}} = -\sum_{\mathrm{PF\ cands.}} \vec{p}_{\mathrm{T}}$;
- $p_{\mathrm{T}}^{\mathrm{miss}} = |\vec{p}_{\mathrm{T}}^{\mathrm{miss}}|$;
- $H_{\mathrm{T}} = \sum_{\mathrm{AK4\ jets}} |\vec{p}_{\mathrm{T}}|$;
- $\Delta\phi_{\mathrm{j},\vec{H}_{\mathrm{T}}^{\mathrm{miss}}}$, the azimuthal angle between the $\vec{p}_{\mathrm{T}}$ of an AK4 jet and $\vec{H}_{\mathrm{T}}^{\mathrm{miss}} = -\sum_{\mathrm{AK4\ jets}} \vec{p}_{\mathrm{T}}$;
- $m_{\mathrm{T}}$, the transverse mass [68] of a system comprising a charged particle track and $\vec{p}_{\mathrm{T}}^{\mathrm{miss}}$; and
- $\Delta R_{\mathrm{Z,b}}$, the angular separation between a wide-cone jet and a b-tagged jet.

The PF candidates appearing in the $\vec{p}_{\mathrm{T}}^{\mathrm{miss}}$ definition are calibrated as explained in Ref. [69]. Similarly, the AK4 jets used for defining $N_{\mathrm{jet}}$, $H_{\mathrm{T}}$ and $\Delta\phi_{\mathrm{j},\,\vec{H}_{\mathrm{T}}^{\mathrm{miss}}}$ must have $|\eta| < 2.4$.

The following requirements define the event selection:

1. $N_{\mathrm{jet}} \geq 2$;
2. $p_{\mathrm{T}}^{\mathrm{miss}} > 300\,\mathrm{GeV}$;
3. $H_{\mathrm{T}} > 400\,\mathrm{GeV}$;
4. $\left|\Delta\phi_{\mathrm{j},\,\vec{H}_{\mathrm{T}}^{\mathrm{miss}}}\right| > 0.5\ (0.3)$ for the first two (up to next two, if $N_{\mathrm{jet}} > 2$) AK4 jets ranked in descending order of $p_{\mathrm{T}}$;
5. no identified isolated photon, electron or muon candidate with $p_{\mathrm{T}} > 10\,\mathrm{GeV}$;
6. no isolated track with $m_{\mathrm{T}} < 100\,\mathrm{GeV}$ and $p_{\mathrm{T}} > 10\,\mathrm{GeV}$ ($p_{\mathrm{T}} > 5\,\mathrm{GeV}$ if the track is identified as a PF electron or muon);
7. at least two AK8 jets with $p_{\mathrm{T}} > 200\,\mathrm{GeV}$;
8. $m_{\mathrm{jet}}$ of the two highest-$p_{\mathrm{T}}$ AK8 jets between 40 and 140 GeV; and
9. $\Delta R_{\mathrm{Z,b}} > 0.8$, for the second-highest-$p_{\mathrm{T}}$ AK8 jet and any b-tagged jet.

The $\Delta\phi_{\mathrm{j},\,\vec{H}_{\mathrm{T}}^{\mathrm{miss}}}$ requirements suppress background from QCD multijet events, as well as hadronic Z and W boson decay events, for which $\vec{H}_{\mathrm{T}}^{\mathrm{miss}}$ is usually aligned along a jet direction. The $m_{\mathrm{T}}$ requirement restricts the isolated track veto to situations consistent with a W boson decay.

The first six requirements define the hadronic baseline, and the last three the selection of events with jet pairs that include pairs of hadronically decaying Z boson candidates. The accepted range in $m_{\mathrm{jet}}$ is chosen to reject the bulk of nonresonant SM processes on the low side, and the peak from boosted top quark jets on the high side, while including sidebands around the Z boson peak to facilitate the determination of background. The $\Delta R_{\mathrm{Z,b}}$ requirement suppresses backgrounds from $\mathrm{t\bar{t}}$ and single top quark events in which a top quark is reconstructed as a b-tagged jet together with a W boson reconstructed as an AK8 jet. This requirement is more efficient for signal than would be a veto of all events with a b-tagged jet.

Figure 2 shows the SM background components for events selected without and with the three Z boson requirements. The main sources of SM background are Z+jets, W+jets, and $\mathrm{t\bar{t}}$. In the case of Z+jets, large $p_{\mathrm{T}}^{\mathrm{miss}}$ comes from $\mathrm{Z} \to \nu\bar{\nu}$. For W+jets, $p_{\mathrm{T}}^{\mathrm{miss}}$ arises from a leptonically decaying W boson where the charged lepton is undetected. Smaller background contributions arise from the QCD multijet events in which jets are under-measured, production of single top quarks, and other SM processes such as diboson production and $\mathrm{t\bar{t}}$ pairs accompanied by vector bosons.

An event satisfying the above criteria lies in the search region (SR) if, in addition, both of the two highest-$p_{\mathrm{T}}$ AK8 jets have $m_{\mathrm{jet}}$ values in the range [70,100] GeV (see Section 6.1 below). Relative to the hadronic baseline selection, about 21% of signal events are retained in the SR, along with 0.5% of background events.

The $p_{\mathrm{T}}^{\mathrm{miss}}$ distribution in the SR is divided into six bins, with lower boundaries at 300, 450, 600, 800, 1000, and 1200 GeV, as shown in Fig. 2.

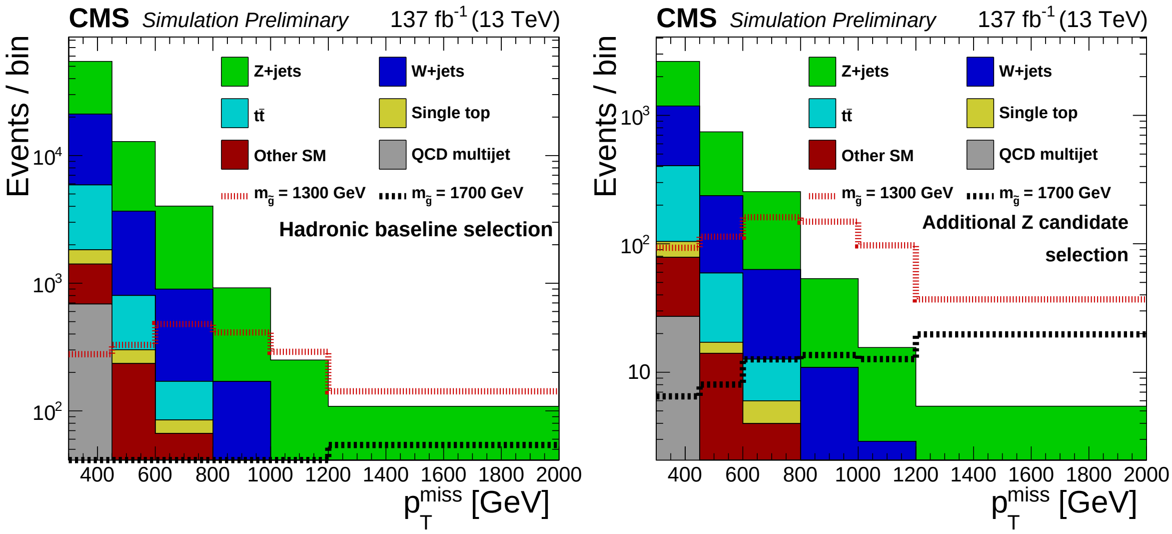


Figure 2: Distributions of $p_{\mathrm{T}}^{\mathrm{miss}}$ for simulated SM backgrounds (stacked histograms), with only the hadronic baseline selection (left), and after the additional Z candidate selection (right). Expected signal contributions for two example mass points (dotted lines) are also shown. The last bin includes overflow events.

# 6 Background estimation method

This section focuses on the estimation of SM backgrounds in each $p_{\mathrm{T}}^{\mathrm{miss}}$ bin. We first describe the data-driven method, then follow with a description of the performance of the method in simulation (MC closure), and the uncertainty in the $p_{\mathrm{T}}^{\mathrm{miss}}$ dependence (shape uncertainty) based on the data observed in the validation samples described in Section 6.3 below.

## 6.1 Data-driven background estimation

Control regions are formed from the events in which one or both of the highest-$p_{\mathrm{T}}$ (leading) and second-highest-$p_{\mathrm{T}}$ (subleading) jets lie in the $m_{\mathrm{jet}}$ sideband $[40, 70] \vee [100, 140]$ GeV. Figure 3 shows the definition of search and control regions in the plane of leading and subleading $m_{\mathrm{jet}}$. Additional control regions are selected by inverting the lepton or photon veto requirement.

The first step of the method is to fit the leading AK8 jet $m_{\mathrm{jet}}$ distribution in the mass sidebands to derive the background normalization integrated over all $p_{\mathrm{T}}^{\mathrm{miss}}$ bins above 300 GeV. This background normalization is denoted by $\mathcal{B}_{\mathrm{norm}}$. We fit the $m_{\mathrm{jet}}$ distriubtion for the leading jet to the mass sideband by excluding the Z signal window, while the subleading jet $m_{\mathrm{jet}}$ is required to be within the Z signal window. The bulk of the background is from nonresonant SM contributions, which can be modeled with a smoothly falling shape. The nominal fit is performed with a linear function as shown in Fig. 4, yielding a total background of $\mathcal{B}_{\mathrm{norm}} =$ 325.0 events.

The uncertainties in $\mathcal{B}_{\mathrm{norm}}$ include a statistical component from the fit, and a systematic one due to the choice of the fitting function. To obtain the statistical uncertainty due to the interpolation of the fit into the SR, pseudoexperiments generated from the background model are fitted with a linear function with the slope and normalization free. The Gaussian width of the resulting distribution of yields in the Z signal window, 10.7 events, is taken as the statistical uncertainty in the total background prediction.

To test if the linear function is adequate to represent the $m_{\mathrm{jet}}$ distribution, we consider higher or-

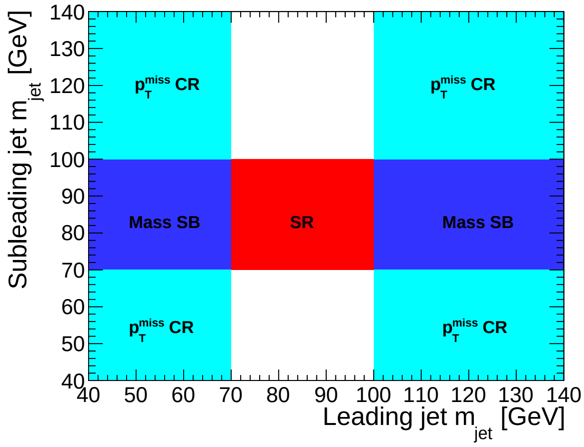


Figure 3: Definition of the search and control regions in the plane of subleading- vs leading-jet $m_{jet}$. The search region (red), with both $m_{jet}$ values lying within the Z signal window, defines the acceptance for potential signal; the leading-jet mass sideband (dark blue), with subleading jet within and leading jet outside the window, is used to measure the background normalization; the $p_T^{miss}$ control region (light blue), with both leading- and subleading-jet $m_{jet}$ values lying outside the Z signal window, is used to derive the $p_T^{miss}$ shape in the search region.

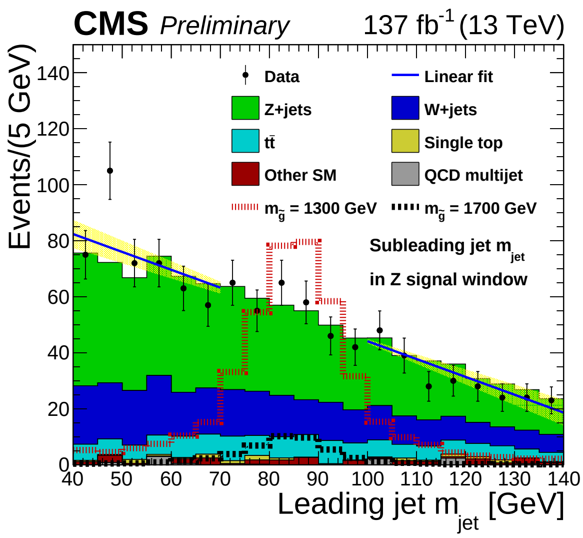


Figure 4: Leading AK8 jet $m_{jet}$ shape fit in the mass sidebands. The Z-candidate selection is applied and the subleading AK8 jet $m_{jet}$ value is required to lie in the Z signal window. The yellow band represents the $\pm 1\sigma$ uncertainty in the fit to the mass sideband performed with a linear function, which is indicated by the blue line. The stacked histogram shows the background from simulation scaled to the data.

der polynomials as alternative functions. We check Chebyshev polynomials of up to the fourth order. The largest variation in the fitted yield with respect to the nominal one, 10.9 events, comes from a fit with a third-order Chebyshev polynomial, and is taken as an additional uncertainty attributable to the fit shape. Considering the statistical uncertainty described above, this results in $\mathcal{B}_{\text{norm}} = 325.0 \pm 15.3$.

To determine the distribution of background events in the $p_{\mathrm{T}}^{\text{miss}}$ bins, we rely on an underlying assumption that $p_{\mathrm{T}}^{\text{miss}}$ and $m_{\text{jet}}$ have minimal correlation. To derive the $p_{\mathrm{T}}^{\text{miss}}$ shape in the SR, a non-overlapping control region (CR) is used in which both leading and subleading AK8 jets have $m_{\text{jet}}$ in the mass sideband. This is referred to as the $p_{\mathrm{T}}^{\text{miss}}$ CR (Fig. 3). In each of the six $p_{\mathrm{T}}^{\text{miss}}$ bins, we calculate the background prediction as

$$\mathcal{B}_i = \mathcal{T} N_i^{\text{CR}}, \tag{1}$$

where $N_i^{\text{CR}}$ is the yield in $p_{\mathrm{T}}^{\text{miss}}$ bin $i$ in the $p_{\mathrm{T}}^{\text{miss}}$ control region, and the transfer factor,

$$\mathcal{T} \equiv \frac{\mathcal{B}_{\text{norm}}}{\sum_i N_i^{\text{CR}}} = 0.198 \pm 0.009, \tag{2}$$

scales the CR yield to that of the SR. The uncertainty in $\mathcal{T}$ includes both statistical and systematic uncertainties in $\mathcal{B}_{\text{norm}}$.

### 6.2 Background closure in simulation

The data-driven background method is tested by applying the procedure to MC simulation in a closure test. We perform this test in two steps.

The main assumption to verify is the lack of correlation between the AK8 jet mass and $p_{\mathrm{T}}^{\text{miss}}$ shape. Figure 5 shows the results of a test of this assumption, where the simulated sample size permits a distribution in relatively fine steps. The plots compare the $p_{\mathrm{T}}^{\text{miss}}$ shape in the search and control regions, for the two main background processes. In both cases we see that the $p_{\mathrm{T}}^{\text{miss}}$ shapes are consistent between the two regions.

For the closure test of the full background method we calculate the background prediction in each $p_{\mathrm{T}}^{\text{miss}}$ bin [Eq. (1)] and compare these predictions with the background yields taken directly from simulation. The results of this test, shown in Fig. 6, demonstrate good agreement within the statistical precision of the test. To account for uncertainties in the comparison, we assign the relative difference between the prediction and direct observation as a non-closure systematic uncertainty in the $p_{\mathrm{T}}^{\text{miss}}$ shape. This difference ranges from 1% to 20%, where the variations in the four lower $p_{\mathrm{T}}^{\text{miss}}$ bins are treated as being anti-correlated with those in the higher $p_{\mathrm{T}}^{\text{miss}}$ bins to give a systematic uncertainty in the $p_{\mathrm{T}}^{\text{miss}}$ shape that does not affect the overall normalization of the background estimation.

### 6.3 $p_{\mathrm{T}}^{\text{miss}}$ shape uncertainty

While the data-driven background estimation method is shown to close well in simulation, we additionally verify in data how well the $p_{\mathrm{T}}^{\text{miss}}$ CR models the $p_{\mathrm{T}}^{\text{miss}}$ shape in the Z signal window. In particular, two validation samples are used to compare the $p_{\mathrm{T}}^{\text{miss}}$ shape obtained from the $p_{\mathrm{T}}^{\text{miss}}$ CR with the one obtained in the Z signal window, used to define our SR, for the main background components. A photon validation sample is used as a proxy for the Z+jets background component, while a single-lepton sample is used to validate the modeling of $\mathrm{t\bar{t}}$ and W+jets combined.

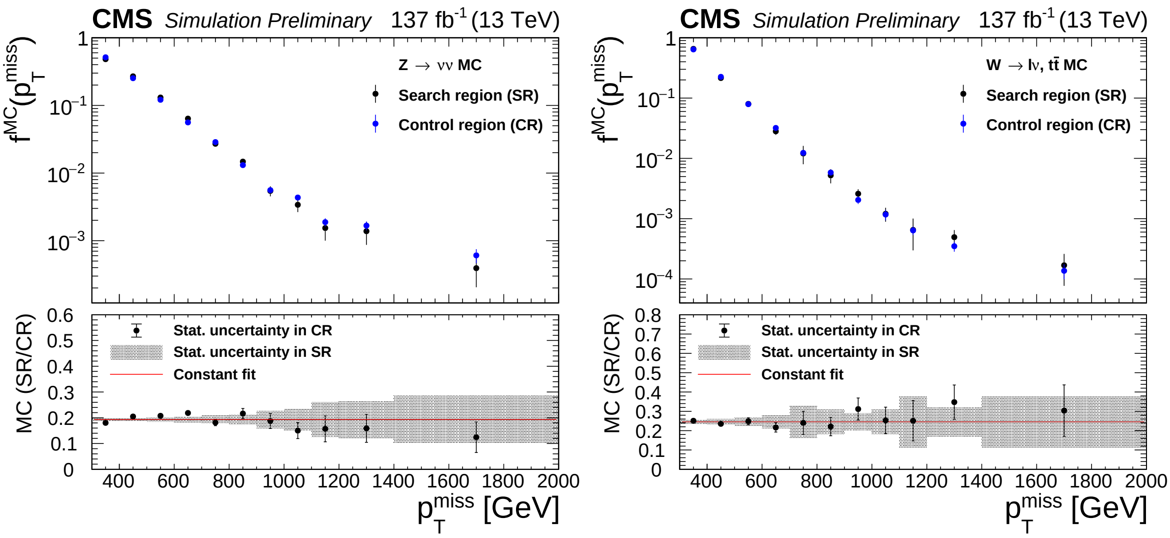


Figure 5: Comparison of the $p_{\mathrm{T}}^{\mathrm{miss}}$ shape in the search and control regions. The top panels show the unit-normalized $p_{\mathrm{T}}^{\mathrm{miss}}$ distributions $f^{\mathrm{MC}}(p_{\mathrm{T}}^{\mathrm{miss}})$ in the two regions while the bottom panels show the ratio of the number of events in the search region to that in the control region. This comparison is done for two main background components: $\mathrm{Z} \to \nu\bar{\nu}$ (left), and $\mathrm{t\bar{t}}$ plus W+jets (right). A fit to a constant is included in the bottom panels to show the average ratio.

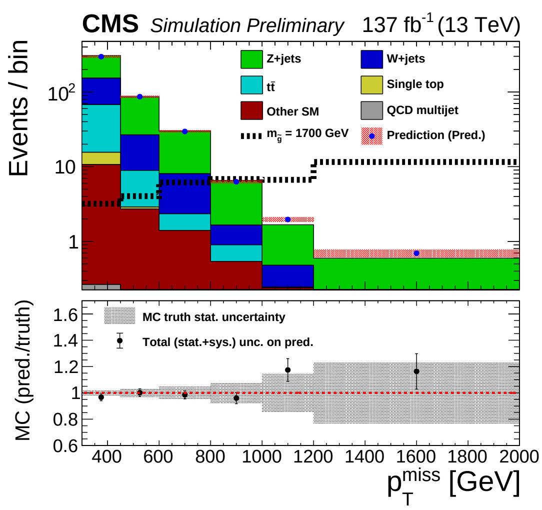


Figure 6: Results of the closure test in which the data-driven prediction method applied to simulation is compared with the direct yield, in the analysis search bins. The lower panel shows the ratio of the prediction to the direct yield. The grey band shows the statistical uncertainty in the direct yield, and the error bars on the points represent the total uncertainty in the prediction.

The photon validation sample is selected from events recorded with a single-photon trigger. The photon $p_T$ is used to emulate the $p_T^{miss}$ from the Z boson when the latter decays to neutrinos. The lower-$p_T$ trigger threshold for the photon compared with the $p_T^{miss}$ threshold in the signal trigger allows us to consider the photon validation sample down to 200 GeV in photon $p_T$ as proxy for $p_T^{miss}$. To enhance the statistics of this sample, we do not require a threshold on $\Delta R_{Z,b}$, since there is a low risk of heavy flavor contamination. All other event selection requirements are the same as for the SR of the analysis.

For the single-lepton sample, the same $p_T^{miss}$ trigger is used as for the SR. The same offline criteria are also applied, with the exception that the $p_T^{miss}$ requirement is relaxed to 200 GeV to gain a longer lever arm for the $p_T^{miss}$ shape comparison.

Figure 7 shows the $p_T^{miss}$ shape comparison for the photon and single-lepton data. Both ratios are consistent with being independent of $p_T^{miss}$ as expected from the MC closure test, albeit within the limited statistical precision of the data. To account for possible shape differences between the search and control regions, we apply a systematic uncertainty in the $p_T^{miss}$ shape based on the difference between a fit to the ratio with a linear function with a floating slope and a flat distribution for both the photon and single-lepton samples. This results in uncertainties ranging from 0–33% on the Z+jets background, which represents 0–28% of the total background, based on the photon validation sample, and 1–14% on the combined $t\bar{t}$ and W+jets background, which represents 0.6–2% of the total background, based on the single-lepton validation sample.

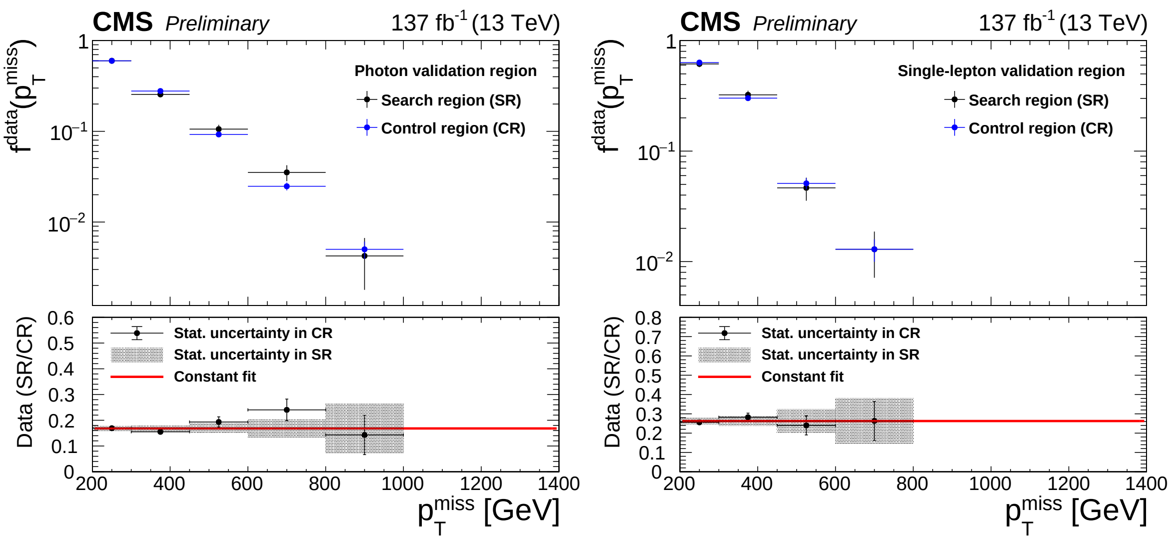


Figure 7: Comparison of the $p_T^{miss}$ shape between the Z signal window and $p_T^{miss}$ control region for the photon (left) and single-lepton (right) validation samples in data. The top panels show the unit-normalized $p_T^{miss}$ distributions $f^{data}(p_T^{miss})$ in the two regions while the bottom panels show the ratio of the number of events in the search region to that in the control region. A fit to a constant is included in the bottom panels to show the average ratio. The horizontal bars on the markers indicate the widths of the search bins.

## 7 Systematic uncertainties

The uncertainties in the SM background prediction are described in Section 6 along with the description of the background estimation method. The uncertainties in the background normalization include the statistical uncertainty from the mass sideband fit interpolation as well as the systematic one derived from alternatative fit functions. The uncertainties in the $p_{\mathrm{T}}^{\mathrm{miss}}$ shape include the $p_{\mathrm{T}}^{\mathrm{miss}}$ CR statistical uncertainties. The systematic uncertainties only affect the $p_{\mathrm{T}}^{\mathrm{miss}}$ shape without changing the background normalization. These are derived from the MC closure and data validation samples. All of these systematic uncertainties are summarized in the upper section of Table 1.

The sources of uncertainty in the signal efficiency affect the signal normalization, the signal $p_{\mathrm{T}}^{\mathrm{miss}}$ shape, or both, as indicated in Table 1. The uncertainty in the luminosity is 2.5% [70], 2.3% [71], and 2.5% [72] for 2016, 2017, and 2018, respectively. The trigger, lepton veto, and isolated-track veto efficiencies are measured in data validation samples and their statistical uncertainties propagated to the signal yields. The ISR modeling in the simulation is adjusted to match the efficiencies measured in $\mathrm{t\bar{t}}$ data events, and the uncertainty in this correction is propagated to the signal yields. To evaluate the uncertainty associated with the renormalization ($\mu_{\mathrm{R}}$) and factorization ($\mu_{\mathrm{F}}$) scales, each scale is varied independently by a factor of 2.0 and 0.5 [73, 74]. Uncertainties in the simulation of pileup are found to be negligible.

The jet momenta in MC samples are smeared to match the jet energy resolution (JER) in data. The jet energy corrections (JECs) are varied using $p_{\mathrm{T}}$- and $\eta$-dependent uncertainties. Both effects are propagated to the jet-dependent variables, including $p_{\mathrm{T}}^{\mathrm{miss}}$, $H_{\mathrm{T}}$, and $\Delta\phi_{\mathrm{j},\vec{H}_{\mathrm{T}}^{\mathrm{miss}}}$, and are varied within the uncertainty of the corrections to derive a systematic uncertainty in the signal yields. The efficiency of the jet quality requirements used to suppress events with misreconstructed jets is found to differ by 1% between data and simulation, and this is applied as a systematic uncertainty. The difference in the resolution of $m_{\mathrm{jet}}$ between data and simulation is applied as a smearing factor to the MC events, and the statistical uncertainty in the size of the correction is included as a systematic uncertainty in the corresponding selection efficiency.

Lastly, the limited precision due to the available statistics in the simulated samples is accounted for as an uncertainty. The systematic uncertainties associated with the signal yields are evaluated assuming that contributions from three years of data-taking (2016, 2017 and 2018) are fully correlated. The total systematic uncertainty in the signal yields ranges from 0.2–6%.

# 8 Results

The background predictions and observed yields for each $p_{\mathrm{T}}^{\mathrm{miss}}$ bin are shown in Table 2 and Fig. 8. The table also gives the inputs to the prediction calculation, Eq. (1). The observations are found to be consistent with the SM predictions within uncertainties, and no evidence for SUSY is observed. We calculate upper limits on the gluino pair-production cross section using a maximum-likelihood fit in which the free parameters are the signal strength $\mu$ and the nuisance parameters associated with the systematic uncertainties in the background and signal model. The uncertainty in the normalization of the background is represented with a log-normal function correlated across all $p_{\mathrm{T}}^{\mathrm{miss}}$ bins, while the $p_{\mathrm{T}}^{\mathrm{miss}}$ CR statistical uncertainties are assigned as uncorrelated. The MC closure and data-MC agreement uncertainties are assigned as correlated across $p_{\mathrm{T}}^{\mathrm{miss}}$ bins.

We evaluate 95% confidence level (CL) upper limits based on the asymptotic form of a likelihood ratio test statistic [75], in conjunction with the $\mathrm{CL_s}$ criterion described in Refs. [76–78]. The test statistic is $q(\mu) = -2\ln(\mathcal{L}_{\mu}/\mathcal{L}_{\max})$, where $\mathcal{L}_{\mu}$ is the maximum likelihood for fixed $\mu$, and $\mathcal{L}_{\max}$ is the same determined by allowing all parameters, including $\mu$, to vary.

Expected and observed 95% CL upper limits, and the predicted gluino pair-production cross

Table 1: Summary of systematic uncertainties, where the ranges refer to different $p_T^{miss}$ bins. In the last column we distinguish uncertainties that affect the normalizations ("norm."), the shapes of distributions, or both.

| Source of uncertainty | Effect on yields (%) | norm. or shape |
|---|---|---|
| Uncertainties in background predictions | | |
| Yield fit statistics | 3.3 | norm. |
| Yield fit shape | 3.4 | norm. |
| $m_{jet}$ CR statistics | 3–100 | shape |
| MC closure | 2–13 | shape |
| Data validation | 2–30 | shape |
| Uncertainties in signal yields | | |
| Luminosity | 2.3–2.5 | norm. |
| Trigger efficiency | 2.0 | both |
| Isolated lepton and track vetos | 2.0 | norm. |
| Jet quality requirements | 1.0 | norm. |
| ISR modeling | 1–2 | both |
| $\mu_R$ and $\mu_F$ scales | 0.2–0.5 | both |
| JEC | 2–4 | both |
| JER | 5–6 | both |
| MC statistics | 1–2 | both |
| AK8 mass resolution | 1–3 | norm. |

sections, are shown in Fig. 9, taking $m(\tilde{\chi}_1^0) = 1\,\text{GeV}$ and $m(\tilde{g}) - m(\tilde{\chi}_2^0) = 50\,\text{GeV}$. This represents a model with a light LSP and a compressed spectrum for the heavy SUSY particles, thereby ensuring a Lorentz-boosted topology. The observed (expected) gluino mass limits reach as high as 1920 (2060) GeV. The observed limit is 1.4 $\sigma$ weaker than the expected one due to the mild excesses observed in the two highest $p_T^{miss}$ bins.

Table 2: Number of events in the $p_T^{miss}$ control region, transfer factor, background prediction, and observed yield in each of the six $p_T^{miss}$ bins. Where two uncertainties are quoted, the first is statistical and the second systematic. The systematic uncertainties in the background prediction include the shape uncertainties in addition to the uncertainty in $\mathcal{T}$. Also listed in the last column is the number of expected signal events and corresponding statistical uncertainties for an example mass point.

| $p_T^{miss}$ bin (GeV) | $p_T^{miss}$ CR yield $N^{CR}$ (events) | Transfer factor $\mathcal{T}$ | Background prediction $\mathcal{B}$ (events) | Observed yield (events) | Exp. signal $m_{\tilde{g}} = 1700$ GeV (events) |
|---|---|---|---|---|---|
| 300 − 450 | 1191 | $0.198 \pm 0.009$ | $236 \pm 7 \pm 16$ | 237 | $3.5 \pm 0.1$ |
| 450 − 600 | 320 | | $63.3 \pm 3.6 \pm 3.3$ | 67 | $4.3 \pm 0.1$ |
| 600 − 800 | 112 | | $22.2 \pm 2.0 \pm 1.9$ | 20 | $6.6 \pm 0.1$ |
| 800 − 1000 | 16 | | $3.17 \pm 0.80 \pm 0.53$ | 3 | $7.2 \pm 0.1$ |
| 1000 − 1200 | 2 | | $0.40 \pm 0.29 \pm 0.11$ | 3 | $7.2 \pm 0.1$ |
| > 1200 | 1 | | $0.20 \pm 0.20 \pm 0.06$ | 1 | $11.6 \pm 0.1$ |

## 9 Summary

Results are presented of a search for events with two hadronically decaying, highly energetic Z bosons and large momentum imbalance, in pp collisions at $\sqrt{s} = 13\,\text{TeV}$. The sample cor-

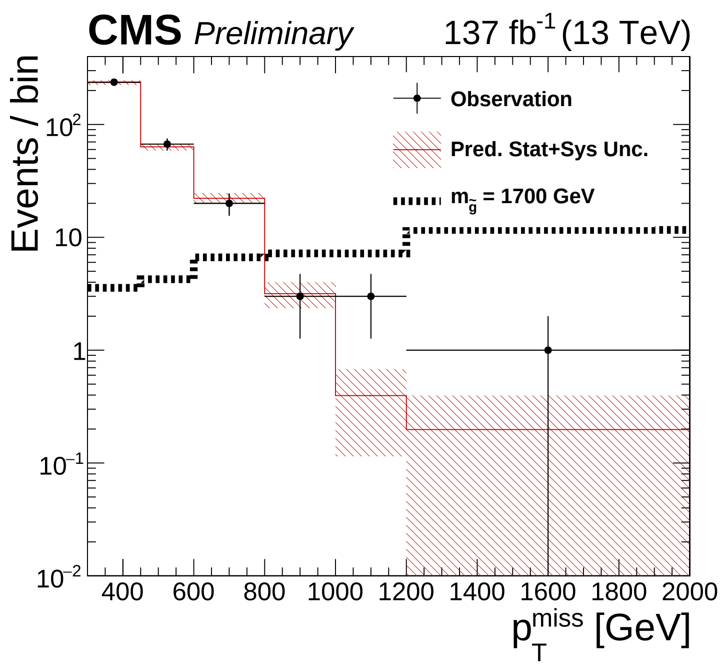


Figure 8: Observation and background prediction as a function of $p_T^{miss}$. The horizontal bar associated with each data point represents the width of the corresponding bin. The red hatched region denotes the expected statistical and systematic uncertainties added in quadrature.

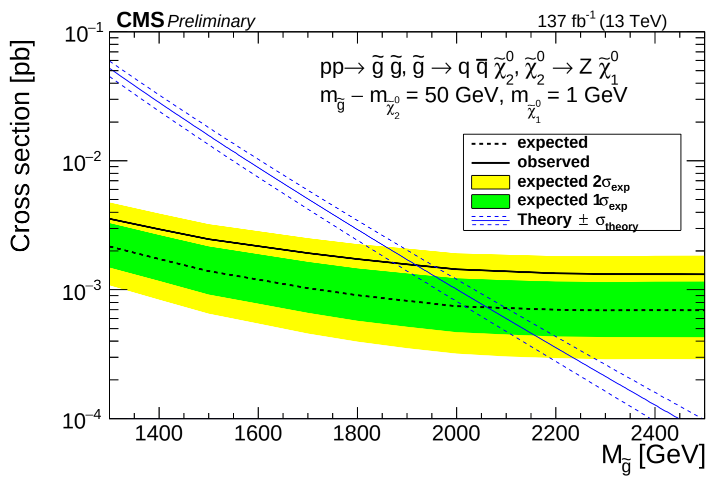


Figure 9: 95% CL upper limit on the production cross section for the T5ZZ signal model as a function of the gluino mass. The thick solid black curve shows the observed exclusion limit. The thick dashed black curve presents the expected limit while the green and yellow bands represent the $\pm1\sigma$ and $\pm2\sigma$ uncertainty ranges. The approximate-NNLO+NNLL cross sections [37–41] are shown in the thin solid blue curve while the dashed blue curves show their theoretical uncertainties [79]. The T5ZZ model assumes a 100% branching fraction for the $\tilde{\chi}_2^0$ to decay to the Z boson and $\tilde{\chi}_1^0$.

responds to an integrated luminosity of 137 $\mathrm{fb}^{-1}$. The signature for a Z boson candidate is a wide-cone jet having a measured mass compatible with the Z boson mass. Yields from standard model background processes are estimated from the data in jet-mass sidebands and other control samples, and are small for events with the largest momentum imbalance. No evidence for physics beyond the standard model is observed. The reach of the search is interpreted in a simplified supersymmetry model of gluino pair production in which each gluino decays to a low-momentum quark pair and the next-to-lightest supersymmetric particle, and the latter decays to a Z boson and the lightest supersymmetric particle. For this scenario, the data exclude gluino masses below 1920 GeV at 95% confidence level.

## References


[1] CMS Collaboration, "Observation of a new boson at a mass of 125 GeV with the CMS experiment at the LHC", *Phys. Lett. B* **716** (2012) 30, doi:10.1016/j.physletb.2012.08.021.

[2] ATLAS Collaboration, "Observation of a new particle in the search for the Standard Model Higgs boson with the ATLAS detector at the LHC", *Phys. Lett. B* **716** (2012) 1, doi:10.1016/j.physletb.2012.08.020.

[3] R. Barbieri and G. F. Giudice, "Upper bounds on supersymmetric particle masses", *Nucl. Phys. B* **306** (1988) 63, doi:10.1016/0550-3213(88)90171-X.

[4] S. Dimopoulos and G. F. Giudice, "Naturalness constraints in supersymmetric theories with nonuniversal soft terms", *Phys. Lett. B* **357** (1995) 573, doi:10.1016/0370-2693(95)00961-J, arXiv:hep-ph/9507282.

[5] R. Barbieri and D. Pappadopulo, "S-particles at their naturalness limits", *JHEP* **10** (2009) 061, doi:10.1088/1126-6708/2009/10/061, arXiv:0906.4546.

[6] M. Papucci, J. T. Ruderman, and A. Weiler, "Natural SUSY endures", *JHEP* **09** (2012) 035, doi:10.1007/JHEP09(2012)035, arXiv:1110.6926.

[7] P. Fayet and S. Ferrara, "Supersymmetry", *Phys. Rept.* **32** (1977) 249, doi:10.1016/0370-1573(77)90066-7.

[8] H. P. Nilles, "Supersymmetry, supergravity and particle physics", *Phys. Rept.* **110** (1984) 1, doi:10.1016/0370-1573(84)90008-5.

[9] S. P. Martin, "A supersymmetry primer", *Adv. Ser. Direct. High Energy Phys.* **21** (2010) 1, doi:10.1142/9789814307505_0001, arXiv:hep-ph/9709356.

[10] P. Fayet, "Supergauge invariant extension of the Higgs mechanism and a model for the electron and its neutrino", *Nucl. Phys. B* **90** (1975) 104, doi:10.1016/0550-3213(75)90636-7.

[11] G. R. Farrar and P. Fayet, "Phenomenology of the production, decay, and detection of new hadronic states associated with supersymmetry", *Phys. Lett. B* **76** (1978) 575, doi:10.1016/0370-2693(78)90858-4.

[12] N. Arkani-Hamed et al., "MARMOSET: The path from LHC data to the new standard model via on-shell effective theories", (2007). arXiv:hep-ph/0703088. https://arxiv.org/abs/hep-ph/0703088.

[13] J. Alwall, M.-P. Le, M. Lisanti, and J. G. Wacker, "Model-independent jets plus missing energy searches", *Phys. Rev. D* **79** (2009) 015005, doi:10.1103/PhysRevD.79.015005, arXiv:0809.3264.

[14] J. Alwall, P. Schuster, and N. Toro, "Simplified models for a first characterization of new physics at the LHC", *Phys. Rev. D* **79** (2009) 075020, doi:10.1103/PhysRevD.79.075020, arXiv:0810.3921.

[15] D. Alves et al., "Simplified models for LHC new physics searches", *J. Phys. G* **39** (2012) 105005, doi:10.1088/0954-3899/39/10/105005, arXiv:1105.2838.

[16] H. Baer et al., "Natural SUSY with a bino- or wino-like LSP", *Phys. Rev. D* **91** (2015) 075005, doi:10.1103/PhysRevD.91.075005.

[17] CMS Collaboration, "The CMS experiment at the CERN LHC", *JINST* **3** (2008) S08004, doi:10.1088/1748-0221/3/08/S08004.

[18] CMS Collaboration, "The CMS trigger system", *JINST* **12** (2017) P01020, doi:10.1088/1748-0221/12/01/P01020, arXiv:1609.02366.

[19] J. Alwall et al., "The automated computation of tree-level and next-to-leading order differential cross sections, and their matching to parton shower simulations", *JHEP* **07** (2014) 079, doi:10.1007/JHEP07(2014)079, arXiv:1405.0301.

[20] J. Alwall et al., "Comparative study of various algorithms for the merging of parton showers and matrix elements in hadronic collisions", *Eur. Phys. J. C* **53** (2008) 473, doi:10.1140/epjc/s10052-007-0490-5, arXiv:0706.2569.

[21] R. Frederix and S. Frixione, "Merging meets matching in MC@NLO", *JHEP* **12** (2012) 061, doi:10.1007/JHEP12(2012)061, arXiv:1209.6215.

[22] P. Nason, "A new method for combining NLO QCD with shower Monte Carlo algorithms", *JHEP* **11** (2004) 040, doi:10.1088/1126-6708/2004/11/040, arXiv:hep-ph/0409146.

[23] S. Frixione, P. Nason, and C. Oleari, "Matching NLO QCD computations with parton shower simulations: the POWHEG method", *JHEP* **11** (2007) 070, doi:10.1088/1126-6708/2007/11/070, arXiv:0709.2092.

[24] S. Alioli, P. Nason, C. Oleari, and E. Re, "A general framework for implementing NLO calculations in shower Monte Carlo programs: the POWHEG BOX", *JHEP* **06** (2010) 043, doi:10.1007/JHEP06(2010)043, arXiv:1002.2581.

[25] S. Alioli, P. Nason, C. Oleari, and E. Re, "NLO single-top production matched with shower in POWHEG: *s*- and *t*-channel contributions", *JHEP* **09** (2009) 111, doi:10.1088/1126-6708/2009/09/111, arXiv:0907.4076. [Erratum: doi:10.1007/JHEP02(2010)011].

[26] E. Re, "Single-top Wt-channel production matched with parton showers using the POWHEG method", *Eur. Phys. J. C* **71** (2011) 1547, doi:10.1140/epjc/s10052-011-1547-z, arXiv:1009.2450.

[27] GEANT4 Collaboration, "GEANT4—a simulation toolkit", *Nucl. Instrum. Meth. A* **506** (2003) 250, doi:10.1016/S0168-9002(03)01368-8.

[28] T. Melia, P. Nason, R. Rontsch, and G. Zanderighi, “$W^+W^-$, WZ and ZZ production in the POWHEG BOX”, *JHEP* **11** (2011) 078, doi:10.1007/JHEP11(2011)078, arXiv:1107.5051.

[29] M. Beneke, P. Falgari, S. Klein, and C. Schwinn, “Hadronic top-quark pair production with NNLL threshold resummation”, *Nucl. Phys. B* **855** (2012) 695, doi:10.1016/j.nuclphysb.2011.10.021, arXiv:1109.1536.

[30] M. Cacciari et al., “Top-pair production at hadron colliders with next-to-next-to-leading logarithmic soft-gluon resummation”, *Phys. Lett. B* **710** (2012) 612, doi:10.1016/j.physletb.2012.03.013, arXiv:1111.5869.

[31] P. Bärnreuther, M. Czakon, and A. Mitov, “Percent level precision physics at the Tevatron: First genuine NNLO QCD corrections to $q\overline{q} \to t\overline{t} + X$”, *Phys. Rev. Lett.* **109** (2012) 132001, doi:10.1103/PhysRevLett.109.132001, arXiv:1204.5201.

[32] M. Czakon and A. Mitov, “NNLO corrections to top-pair production at hadron colliders: the all-fermionic scattering channels”, *JHEP* **12** (2012) 054, doi:10.1007/JHEP12(2012)054, arXiv:1207.0236.

[33] M. Czakon and A. Mitov, “NNLO corrections to top pair production at hadron colliders: the quark-gluon reaction”, *JHEP* **01** (2013) 080, doi:10.1007/JHEP01(2013)080, arXiv:1210.6832.

[34] M. Czakon, P. Fiedler, and A. Mitov, “Total top-quark pair-production cross section at hadron colliders through $O(\alpha_S^4)$”, *Phys. Rev. Lett.* **110** (2013) 252004, doi:10.1103/PhysRevLett.110.252004, arXiv:1303.6254.

[35] R. Gavin, Y. Li, F. Petriello, and S. Quackenbush, “W physics at the LHC with FEWZ 2.1”, *Comput. Phys. Commun.* **184** (2013) 208, doi:10.1016/j.cpc.2012.09.005, arXiv:1201.5896.

[36] R. Gavin, Y. Li, F. Petriello, and S. Quackenbush, “FEWZ 2.0: A code for hadronic Z production at next-to-next-to-leading order”, *Comput. Phys. Commun.* **182** (2011) 2388, doi:10.1016/j.cpc.2011.06.008, arXiv:1011.3540.

[37] W. Beenakker, R. Höpker, M. Spira, and P. M. Zerwas, “Squark and gluino production at hadron colliders”, *Nucl. Phys. B* **492** (1997) 51, doi:10.1016/S0550-3213(97)00084-9, arXiv:hep-ph/9610490.

[38] A. Kulesza and L. Motyka, “Threshold resummation for squark-antisquark and gluino-pair production at the LHC”, *Phys. Rev. Lett.* **102** (2009) 111802, doi:10.1103/PhysRevLett.102.111802, arXiv:0807.2405.

[39] A. Kulesza and L. Motyka, “Soft gluon resummation for the production of gluino-gluino and squark-antisquark pairs at the LHC”, *Phys. Rev. D* **80** (2009) 095004, doi:10.1103/PhysRevD.80.095004, arXiv:0905.4749.

[40] W. Beenakker et al., “Soft-gluon resummation for squark and gluino hadroproduction”, *JHEP* **12** (2009) 041, doi:10.1088/1126-6708/2009/12/041, arXiv:0909.4418.

[41] W. Beenakker et al., “Squark and gluino hadroproduction”, *Int. J. Mod. Phys. A* **26** (2011) 2637, doi:10.1142/S0217751X11053560, arXiv:1105.1110.

[42] W. Beenakker et al., "NNLL-fast: predictions for coloured supersymmetric particle production at the LHC with threshold and Coulomb resummation", *JHEP* **12** (2016) 133, doi:10.1007/JHEP12(2016)133, arXiv:1607.07741.

[43] W. Beenakker et al., "NNLL resummation for squark-antisquark pair production at the LHC", *JHEP* **01** (2012) 076, doi:10.1007/JHEP01(2012)076, arXiv:1110.2446.

[44] W. Beenakker et al., "Towards NNLL resummation: hard matching coefficients for squark and gluino hadroproduction", *JHEP* **10** (2013) 120, doi:10.1007/JHEP10(2013)120, arXiv:1304.6354.

[45] W. Beenakker et al., "NNLL resummation for squark and gluino production at the LHC", *JHEP* **12** (2014) 023, doi:10.1007/JHEP12(2014)023, arXiv:1404.3134.

[46] W. Beenakker et al., "Stop production at hadron colliders", *Nucl. Phys. B* **515** (1998) 3, doi:10.1016/S0550-3213(98)00014-5, arXiv:hep-ph/9710451.

[47] W. Beenakker et al., "Supersymmetric top and bottom squark production at hadron colliders", *JHEP* **08** (2010) 098, doi:10.1007/JHEP08(2010)098, arXiv:1006.4771.

[48] W. Beenakker et al., "NNLL resummation for stop pair-production at the LHC", *JHEP* **05** (2016) 153, doi:10.1007/JHEP05(2016)153, arXiv:1601.02954.

[49] T. Sjöstrand et al., "An introduction to PYTHIA 8.2", *Comput. Phys. Commun.* **191** (2015) 159, doi:10.1016/j.cpc.2015.01.024, arXiv:1410.3012.

[50] CMS Collaboration, "Event generator tunes obtained from underlying event and multiparton scattering measurements", *Eur. Phys. J. C* **76** (2016) 155, doi:10.1140/epjc/s10052-016-3988-x, arXiv:1512.00815.

[51] CMS Collaboration, "Extraction and validation of a new set of CMS PYTHIA8 tunes from underlying-event measurements", *Eur. Phys. J. C* **80** (2020) 4, doi:10.1140/epjc/s10052-019-7499-4, arXiv:1903.12179.

[52] NNPDF Collaboration, "Parton distributions with QED corrections", *Nucl. Phys. B* **877** (2013) 290, doi:10.1016/j.nuclphysb.2013.10.010, arXiv:1308.0598.

[53] NNPDF Collaboration, "Parton distributions from high-precision collider data", *Eur. Phys. J. C* **77** (2017) 663, doi:10.1140/epjc/s10052-017-5199-5, arXiv:1706.00428.

[54] CMS Collaboration, "Particle-flow reconstruction and global event description with the CMS detector", *JINST* **12** (2017) P10003, doi:10.1088/1748-0221/12/10/P10003, arXiv:1706.04965.

[55] M. Cacciari, G. P. Salam, and G. Soyez, "The anti-$k_T$ jet clustering algorithm", *JHEP* **04** (2008) 063, doi:10.1088/1126-6708/2008/04/063, arXiv:0802.1189.

[56] M. Cacciari, G. P. Salam, and G. Soyez, "FastJet user manual", *Eur. Phys. J. C* **72** (2012) 1896, doi:10.1140/epjc/s10052-012-1896-2, arXiv:1111.6097.

[57] CMS Collaboration, "Jet performance in pp collisions at $\sqrt{s} = 7$ TeV", CMS Physics Analysis Summary CMS-PAS-JME-10-003, CERN, 2010.

[58] CMS Collaboration, “Jet algorithms performance in 13 TeV data”, CMS Physics Analysis Summary CMS-PAS-JME-16-003, CERN, 2017.

[59] CMS Collaboration, “Jet energy scale and resolution in the CMS experiment in pp collisions at 8 TeV”, *JINST* **12** (2017) P02014, doi:10.1088/1748-0221/12/02/P02014, arXiv:1607.03663.

[60] M. Cacciari and G. P. Salam, “Pileup subtraction using jet areas”, *Phys. Lett. B* **659** (2008) 119, doi:10.1016/j.physletb.2007.09.077, arXiv:0707.1378.

[61] A. J. Larkoski, S. Marzani, G. Soyez, and J. Thaler, “Soft Drop”, *JHEP* **05** (2014) 146, doi:10.1007/JHEP05(2014)146, arXiv:1402.2657.

[62] D. Bertolini, P. Harris, M. Low, and N. Tran, “Pileup Per Particle Identification”, *JHEP* **10** (2014) 059, doi:10.1007/JHEP10(2014)059, arXiv:1407.6013.

[63] CMS Collaboration, “Identification of heavy-flavour jets with the CMS detector in pp collisions at 13 TeV”, *JINST* **13** (2018) P05011, doi:10.1088/1748-0221/13/05/P05011, arXiv:1712.07158.

[64] CMS Collaboration, “Performance of electron reconstruction and selection with the CMS detector in proton-proton collisions at $\sqrt{s} = 8\,\text{TeV}$”, *JINST* **10** (2015) P06005, doi:10.1088/1748-0221/10/06/P06005, arXiv:1502.02701.

[65] CMS Collaboration, “Performance of the CMS muon detector and muon reconstruction with proton-proton collisions at $\sqrt{s} = 13\,\text{TeV}$”, *JINST* **13** (2018) P06015, doi:10.1088/1748-0221/13/06/P06015, arXiv:1804.04528.

[66] K. Rehermann and B. Tweedie, “Efficient identification of boosted semileptonic top quarks at the LHC”, *JHEP* **03** (2011) 059, doi:10.1007/JHEP03(2011)059, arXiv:1007.2221.

[67] CMS Collaboration, “Performance of photon reconstruction and identification with the CMS detector in proton-proton collisions at $\sqrt{s} = 8\,\text{TeV}$”, *JINST* **10** (2015) P08010, doi:10.1088/1748-0221/10/08/P08010, arXiv:1502.02702.

[68] UA1 Collaboration, “Experimental observation of isolated large transverse energy electrons with associated missing energy at $\sqrt{s} = 540$ GeV”, *Phys. Lett. B* **122** (1983) 103, doi:10.1016/0370-2693(83)91177-2.

[69] CMS Collaboration, “Performance of missing transverse momentum reconstruction in proton-proton collisions at $\sqrt{s} = 13$ TeV using the CMS detector”, *JINST* **14** (2019) P07004, doi:10.1088/1748-0221/14/07/P07004, arXiv:1903.06078.

[70] CMS Collaboration, “CMS luminosity measurements for the 2016 data taking period”, CMS Physics Analysis Summary CMS-PAS-LUM-17-001, CERN, 2017.

[71] CMS Collaboration, “CMS luminosity measurement for the 2017 data-taking period at $\sqrt{s} = 13$ TeV”, CMS Physics Analysis Summary CMS-PAS-LUM-17-004, CERN, 2018.

[72] CMS Collaboration, “CMS luminosity measurement for the 2018 data-taking period at $\sqrt{s} = 13$ TeV”, CMS Physics Analysis Summary CMS-PAS-LUM-18-002, CERN, 2019.

[73] S. Catani, D. de Florian, M. Grazzini, and P. Nason, “Soft gluon resummation for Higgs boson production at hadron colliders”, *JHEP* **07** (2003) 028, doi:10.1088/1126-6708/2003/07/028, arXiv:hep-ph/0306211.

[74] M. Cacciari et al., "The $t\bar{t}$ cross-section at 1.8 TeV and 1.96 TeV: a study of the systematics due to parton densities and scale dependence", *JHEP* **04** (2004) 068, doi:10.1088/1126-6708/2004/04/068, arXiv:hep-ph/0303085.

[75] G. Cowan, K. Cranmer, E. Gross, and O. Vitells, "Asymptotic formulae for likelihood-based tests of new physics", *Eur. Phys. J. C* **71** (2011) 1554, doi:10.1140/epjc/s10052-011-1554-0, arXiv:1007.1727. [Erratum: doi:10.1140/epjc/s10052-013-2501-z].

[76] A. L. Read, "Presentation of search results: the $CL_s$ technique", *J. Phys. G* **28** (2002) 2693, doi:10.1088/0954-3899/28/10/313.

[77] T. Junk, "Confidence level computation for combining searches with small statistics", *Nucl. Instrum. Meth. A* **434** (1999) 435, doi:10.1016/S0168-9002(99)00498-2, arXiv:hep-ex/9902006.

[78] ATLAS and CMS Collaborations, "Procedure for the LHC Higgs boson search combination in Summer 2011", Technical Report CMS-NOTE-2011-005, ATL-PHYS-PUB-2011-11, CERN, 2011.

[79] C. Borschensky et al., "Squark and gluino production cross sections in pp collisions at $\sqrt{s}$ = 13, 14, 33 and 100 TeV", *Eur. Phys. J. C* **74** (2014) 3174, doi:10.1140/epjc/s10052-014-3174-y, arXiv:1407.5066.